RESEARCH PAPER

Effects of Plasticity on Patched and Unpatched Center Crack Tension Specimens

D.C. Hart [1,2] · H.A. Bruck [2]

Abstract

Composite patch repairs of aluminum structures are designed using linear elastic fracture mechanics, which compares crack tip predictions to a critical strain energy release rate or stress intensity. Analytical and numerical predictions are reasonable for linear-elastic behavior, but do not account for the elastic-plastic behavior observed at the crack tip of ductile materials below the ultimate load. This research used digital image correlation to study full field displacements and strains ahead of the crack tip for unpatched and patched center crack tension specimens loaded monotonically to failure. Both qualitative and quantitative comparisons show measureable effects of surface reinforcement on crack tip behavior. Free surface fracture response was an intrinsic property of the aluminum from the initial development of the plastic strain zone through crack blunting and ultimately through peak load with all stages occurring at crack opening displacements (COD) independent of the one-sided composite patch reinforcement. Patch reinforcement increased the ultimate tensile load 160% and the total achieved COD by 20% over the unpatched behavior. Increased capacity was related to an increase in accumulated large strain area and distributed plasticity measured on the free surface prior to the end of crack blunting. The direct correlation of fracture behavior indicates patched specimen failure can be predicted using unpatched specimen COD.

Keywords Composite patch · Aluminum · 5052-H32 · Digital image correlation · Center crack tension

Introduction

The foundation of bonded joint design was first introduced in the late 1930's and 1940's with the governing differential equations for an explicit adhesive layer [1, 2], and later advanced when Hart-Smith introduced inelastic behavior of the adhesive layer [3, 4]. The application of bonded joint design in the development of aircraft patch repairs continued to evolve through a combination of mechanical characterization protocols, development of appropriate design methods based on adhesive and adherend governing equations, and enhancement of analysis efforts [5–7] by incorporating linear elastic fracture mechanics (LEFM) to calculate either strain energy release rate

(SERR) or stress intensity (K) at the metallic crack tip. When extending the design approach for 2D joints to include the crack tip of one-sided composite patch repaired aluminum Wang and Rose utilized a distribution of springs to represent the load bridging and plate theory with a linear elastic energy balance to couple normal and bending stress components to crack tip stress intensity [8, 9]. Advancements in computational algorithms, particularly Finite Element Analysis techniques such as Virtual Crack Closure, simplified the development of numerical analysis approaches [10–12]. However, as the thickness and ductility of the repaired plate increases the inelastic failure mechanisms play significant roles in the ultimate load capacity of the repaired plate, which neither the analytical nor the numerical methods account for.

Low modulus composite patches have been used to address stress corrosion cracking of marine grade aluminum deck plating in U.S. Navy applications [10, 13]. Access to the damaged plate is typically limited to one side, and the application of the patch requires limited heat input to minimize residual stress due to the resin cure temperature and the difference in coefficients of thermal expansion. Recent testing of one-sided low

✉ D.C. Hart
daniel.c.hart@navy.mil

1 Naval Surface Warfare Center, Naval Sea Systems Command, Carderock, MD, USA

2 Department of Mechanical Engineering, University of Maryland, College Park, MD, USA
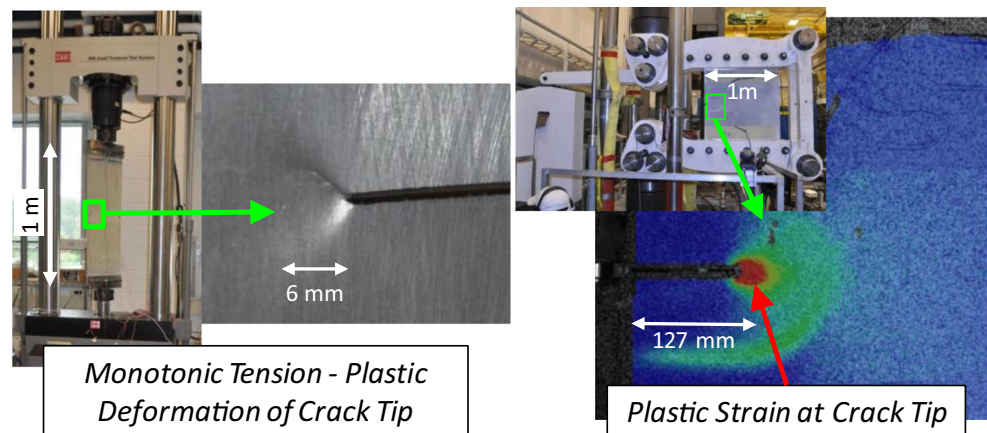
modulus composite patched center crack tension (CCT) and large-scale ductile tearing specimens [13–15] have demonstrated increased monotonic load and displacement capacity compared with the unpatched specimens. A common failure mechanism observed was significant plastic deformation of the aluminum ahead of the crack tip. Large-scale testing of one-sided patched aluminum specimens, shown in Fig. 1, has shown that the elastic-plastic crack tip behavior occurs before ultimate failure [10, 13]. Hutchinson, Rice, and Rosengren (HRR) [16–18] established the J-integral method and the stress, strain, and displacements fields to describe inelastic crack tip behavior for ductile metals. To characterize the full-field crack tip behavior, Digital Image Correlation (DIC) [19] can be utilized to measure surface displacements ahead of the crack tip. Initially utilized for local linear elastic material behavior [20, 21], inelastic material behavior can be included in the J-integral calculation [22–24]. Research in the plastic zone development under monotonic loading appears to be limited to typical monolithic fracture mechanics specimens [25, 26]. Dadkhah and Kobyashi reported displacements and J-integral data with comparison to the HRR displacement fields under static and fatigue crack growth conditions on thin 5052-H32 sheet [27, 28]. Additional work with 6061-T6 and various tempers of 2024 aluminum has been reported [29, 30].

The focus of this research is on how a one-sided adhesively bonded low modulus E-Glass/Epoxy composite patch affects development of the crack tip plastic zone for small-scale cracked aluminum CCT specimens loaded monotonically in tension until failure. Full field 2D DIC data from the free aluminum surface for both unpatched and patched specimens will be compared from initial linear elastic loading response through plastic zone development, the crack blunting stage, and ultimate failure to improve our understanding of the one-sided surface reinforcement effects on crack tip material behavior. This research builds the foundation for future research focused on predicting failure of low modulus composite patches.

Experimental Procedure

The test frame, DIC setup, typical speckle pattern, and specimen configuration are shown in Fig. 2. Small-scale CCT specimen geometry was selected for manufacturing and testing convenience as well as maintaining a configuration link to the large-scale testing performed by Hart et al. [10, 15]. Readily available 2.29 mm thick marine grade 5052-H32 aluminum was selected. Small-scale CCT specimen blank plates were 24 mm wide (2 W) and 114 mm long with electrical discharge machined (EDM) notches nominally 12 mm wide and 0.36 mm high. Sharp crack tips were then grown from the notch using high cycle low load tension-tension fatigue. The load ratio (R) was 0.1 for a tensile load that varied from 200 to 2000 N at 10 Hz. The resulting effective ΔK was nominally between 5.6 and 6.7 MPa-$\sqrt{m}$, which resulted in a nominal cycle count of 100 K to achieve 1 mm of crack growth. With sharp crack tips and a crack length (2a) of 14 mm the specimens were paired by crack length and one of each pair received an adhesively bonded composite patch. Surface preparation involved an acetone wipe, light surface abrasion with 80 grit aluminum oxide sandpaper, a second acetone wipe, and then treatment with 3M's AC-130-2 bonding agent. A commercially available marine adhesive, West Systems WestSix10, was selected for bonding the pre-fabricated 0/90 E-Glass epoxy laminate. Nominal linear elastic tensile properties for the adhesive and laminate were reported by Hart et al. [31]. The woven E-glass laminate had an average thickness of 1.27 mm cut to 50 mm long by 24 mm wide with fiber reinforcement in both the 0- and 90-degree directions. The composite patch was centered on the machined notch and bonded to plate using 0.6 mm diameter steel welding wire to control bondline thickness. Because the objective was to study plastic zone development and not optimization of the patch for ultimate load capacity, no effort was made to machine or taper the patch ends to reduce adhesive peel stress at the crack tip and increase load capacity.

Fig. 1 Plastic zone on free surface of 28 × 92 cm large-scale patched CCT (L) and 1 m² ductile tearing (R) specimens

1 m

6 mm

Monotonic Tension - Plastic Deformation of Crack Tip

1m

127 mm

Plastic Strain at Crack Tip

Fig. 2 Small scale CCT test frame and DIC configuration (L), FOV (C), and CCT specimen geometry (R)

Free Surface DIC Speckle Pattern and FOV
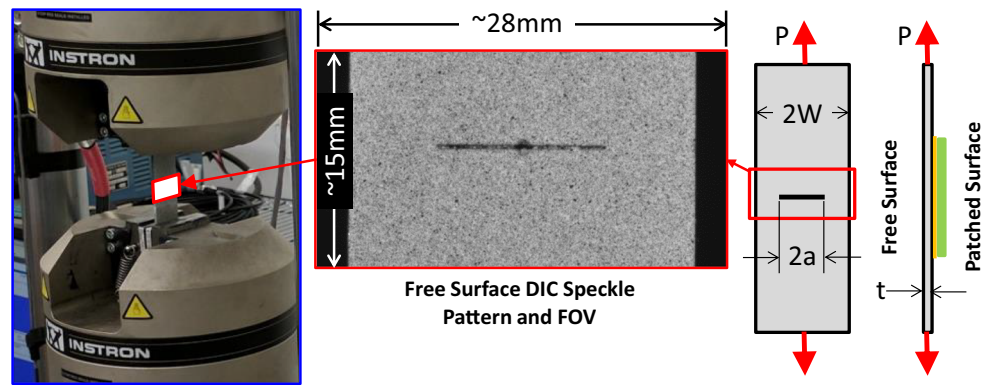
Tensile testing was performed on a 20 kip 4-post hydraulic MTS frame with Instron hydraulic wedge grips and controls. Loading was applied at a rate of 0.18 mm/min until beyond the linear elastic response range when the non linear load response slope stabilized in the crack blunting region and the loading rate was doubled. Data acquisition included machine load and static images for DIC. Images were taken using a Point Grey Flea FL3-U3-88S2C-C camera with a Tamron 28–80 mm f/3.5–22 lens resulting in a 28.2 mm × 14.9 mm field of view (FOV). Initial depth of field (DoF) was set so the free surface remained in focus for the range of out-of-plane deflection experienced minimizing bias error due to movement relative to the camera lens. Out-of-plane displacement was estimated as 0.36 mm, the difference in the load line through the aluminum plate and the aluminum/composite centroid, and is assumed to not warrant the use of 3D DIC. The speckle pattern was obtained using a base of flat white spray paint with speckles applied by letting flat black spray paint fog settle on the white surface. The fog process was repeated until sufficient gray scale information was present in the image. High contrast images were achieved using two evenly spaced 250 watt halogen spot lights; lights were equidistant from the grip bodies, equidistant to the camera body, and level with the camera body and specimen. Images were processed using Correlated Solutions Inc. Vic-2D version 6 software [32], a subset size of 51 × 51 pixels (0.35 × 0.35 mm), and a step size of 10 pixels (0.069 mm). Displacements are a direct measurement between correlated subsets while strains are determined from shape functions that describe displacement and rotation across the subset. The shape function coefficients are optimized by minimizing the sum of the squares error of predicted and correlated displacements and rotations of each subset. Strains, in this case the Lagrangian finite strain tensor defined by equation (1), are calculated with a 90% center-weighted Gaussian filter with a 31 data point window size then smoothed using the same filter across 15 data points. Subset, step, filter, and smoothing parameters were selected by comparing the correlation match confidence interval, strain magnitude change, strain error, and strain bias

from an initial reference image set taken with the specimen held at zero load. During the linear elastic response range images were taken at 2 per second, as the response advanced into the crack blunting stage the image rate was decreased then increased to the original speed prior to crack growth and failure.

$$\varepsilon_{\alpha,\beta} = \frac{1}{2}\left(u_{\alpha,\beta} + u_{\beta,\alpha} + u_{\gamma,\beta}u_{\gamma,\alpha}\right) \quad (1)$$

Experimental Results

Comparison of Patched and Unpatched Specimen Response

The data reported in this paper is limited to two unpatched and two patched specimens. Load versus crack opening displacement (COD) response due to monotonic tensile loading was consistent between like specimens, where COD is measured using DIC displacements across the machined notch on the free surface. Unprocessed static images were used to identify stages of failure progression from the linear elastic response through crack blunting and then finally crack growth until specimen failure. Displacement and strain data were calculated using VIC 2D software. Load response with crack stage progression is shown in Fig. 3 and the DIC measured average von Mises strain ahead of the crack tip versus COD is shown in Fig. 4. Free surface 2D von Mises strain measurements are defined using equation (2) and was studied because the von Mises yield criterion and equivalent stress are the foundation of plastic zone shape approximations and Irwin's plastic radius approximation.

$$\varepsilon_{vm} = \sqrt{\varepsilon_1^2 - \varepsilon_1\varepsilon_2 + \varepsilon_2^2} \quad (2)$$

The data indicates crack stage progression on the free surface for both patched and unpatched specimens occurs at corresponding CODs. Crack blunting is assumed based on unprocessed and DIC processed static images of the
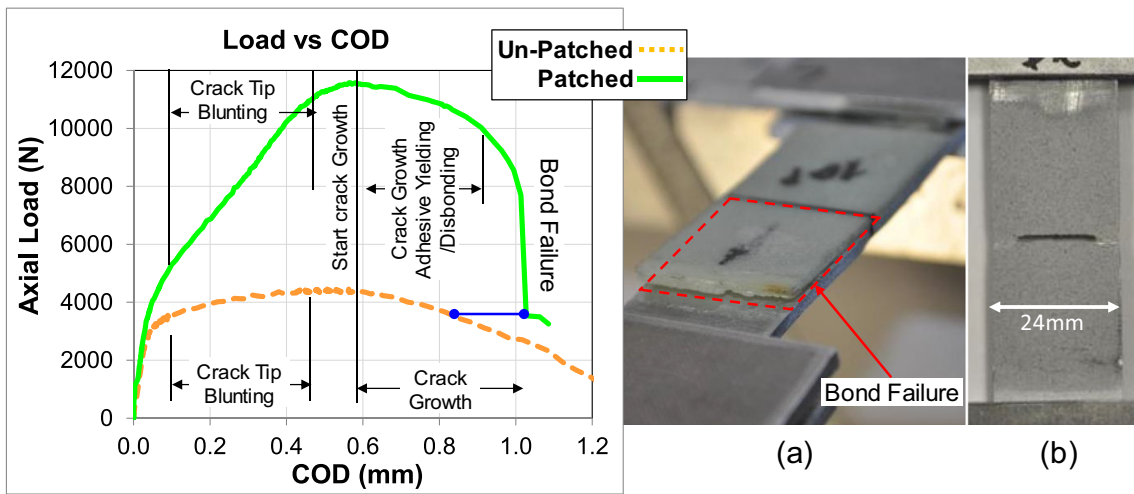
Fig. 3 Load response showing consistent behavior as a function of COD with failure modes of a tested patched (**a**) and unpatched (**b**) specimen

free surface crack tip where displacement and rotation of the material relative to the crack tip occurs after plastic 2D von Mises strain is measured and without extension of the crack. For both unpatched and patched specimens blunting behavior occurs from just beyond the elastic response limit, at a COD of 0.11 mm, to a COD of 0.41 mm. Beyond crack blunting material behavior ahead of the crack transitions into crack growth prior to peak loads at a COD of 0.57 mm, at which point the load is 160% greater for the patched specimen. Evidence of patch disbonding occurs in unprocessed static digital images used for DIC where adhesive was visible through the notch. When the patch adjacent to the notch is fully bonded, relative displacement between successive images was not detectable. During the crack growth and adhesive yielding response, prior to the load drop, sudden relative displacement between the notch and adhesive is visible and coincides with initiation of the load drop indicating disbonding of the patch. Based on observations made during testing and static images, adhesive yielding and failure continues until bond failure of half the patch, at which point the crack growth behavior is only that of the

aluminum. The right side of Fig. 3 shows the final disbond of half the patch (a) along with the failed aluminum specimen (b). When comparing post peak load aluminum fracture at 3500 N, the load level after patch failure, the COD is 20% greater for the patched specimen, as shown by the blue line in Fig. 3. This additional 0.2 mm of COD on the free surface is related to the plastic material behavior ahead of the crack tip, which is partially constrained by the one-sided bonded patch reinforcement.

Comparison of free surface von Mises strain behaviors of unpatched and patched specimens as a function of COD is shown in Fig. 4. Simply for comparison purposes, the 2D von Mises strain values plotted are averaged over a 1 mm^2 region nominally 1 mm ahead of the crack tip. The strain behaviors ahead of the crack tip were nearly identical for COD values less than 0.3 mm, at which point adhesive plasticity is assumed to begin playing a role in the response of the patched specimen. When the COD is greater than 0.3 the slope of the von Mises strain versus the COD of the patched specimen is lower than the unpatched specimen, which is presumed related to an increase in the region of plastic shear stress in the adhesive layer. Near peak load, COD of

Fig. 4 Total von Mises strain data ahead of the crack tip showing adhesive plasticity and patch failure
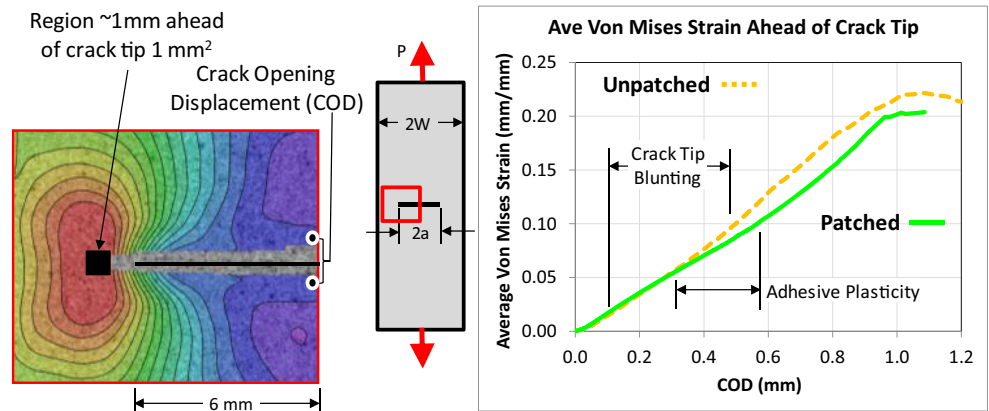
0.55 mm, the slope of the local strain response is the same for unpatched and patched specimens though there is a COD offset. Unpatched aluminum exhibits tearing and a gradual drop in load near failure. Composite patched specimen load decreases with a combination of crack growth and disbonding until full bondline failure resulting in a large load drop. As the composite patch bond fails and no longer reinforces the aluminum, free surface strains are similar to those for unpatched aluminum.

At COD magnitudes below 0.02 mm the load versus COD response of the specimen is linear elastic. Von Mises strain contours in Fig. 5 are showing greater strain magnitude and large strain region due to out-of-plane bending. In the linear elastic region, the out-of-plane bending increases until the load passes through the neutral axis of the patched specimen. During the bending response the surface strain of the composite patched specimen increases at a greater rate than the unpatched specimen, which only experiences an in-plane tensile material response.

Once the load axis aligns with the neutral axis of the specimen both the unpatched and patched strains increase at similar rates. Strain contours for a COD of 0.2 mm, early stage of crack blunting, are shown Fig. 6. High levels of strain for the unpatched specimen are focused at the crack tip with large strains showing the influence of edge effects and ligament tensile behavior. Strain contours for the patched specimen indicate a measureable effect of the surface reinforcement with a blunted region of large strain ahead of the crack tip with a greater area of large strain, consistent with fiber reinforcement in both axial and transverse directions. The increase in the area of large strain associated with patching is assumed to contribute to the 20% increase in COD when comparing specimen response at matching load levels after the patch fails. A quantification of the strain area is required to verify this result.

Crack Tip Grain Structure

A deeper understanding of the material at the crack tip is required to study the formation of the plastic zone ahead of the crack tip singularity, which is assumed to be asymptotic as a function of $1/\sqrt{r}$ [17]. A microscopic study of the surface grain structure was performed to establish homogenous isotropic material behavior relative to macro level material response prior to crack growth. Only limited image processing was performed to confirm grain size, as the aluminum is assumed to be fine grained without texture.

Cold work hardened 5××× series aluminum alloy contains center face cubic crystals with $(FE,CR)_3SiAl_{12}$, Mg_2Si, and Magnesium as Mg_2Al_3 at concentrations between 2.2 and 2.8% [33, 34]. One characteristic of these alloys are grains that have been elongated and oriented with the rolling direction during cold work. Grain structure, which determines how stresses are carried, was studied using a light optical microscope (LOM) at a magnification level of 5× and 20×. Images were taken of the long transverse (L-T) surface, as defined in ASTM E399 [35], corresponding to crack plane alignment of the CCT specimens. The intermetallics, visible in the microscope image in Fig. 7, indicate the rolling direction. For grain structure images samples of the aluminum plate were polished, electro-chemically etched following ASTM E407 [36], and imaged using a LOM with a gamma filter and polarized light. Samples were cut, and then potted with a pure nickel wire protruding from one surface. Each specimen was then mechanically wet sanded and polished in stages from 120 grit to an active oxide polishing OP-U 0.04 μm colloidal silica solution. Directly following the last polishing step specimens were electro-chemically etched using Barker's Reagent (5% HBF solution) and an electric current. With the sample suspended 10–15 mm below the surface of the solution a 20 VDC was applied between a stainless steel cathode in the

Fig. 5 Von Mises strain contour comparison for a COD = 0.02 mm in the linear elastic response range showing influence of bending on patched specimen surface strains
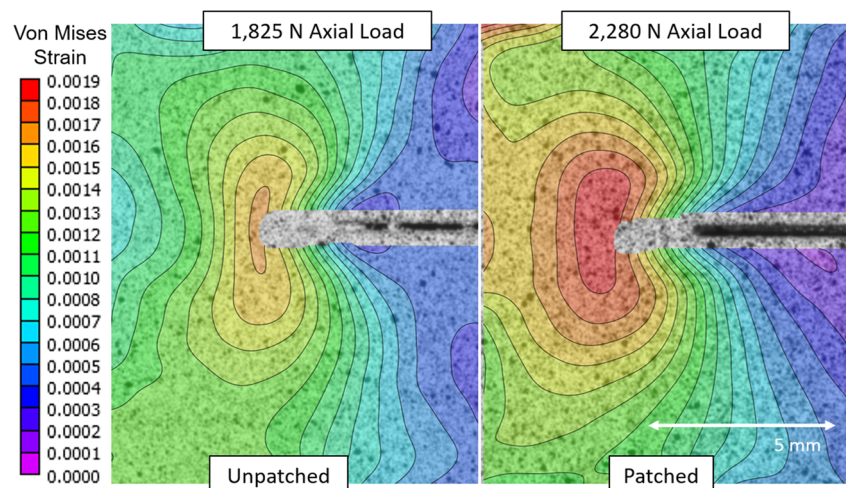
Fig. 6 Von Mises strain comparison of unpatched (L) and patched (R) crack tips during the early stage of crack blunting (COD = 0.2 mm) showing increased area of large strain for the patched specimen
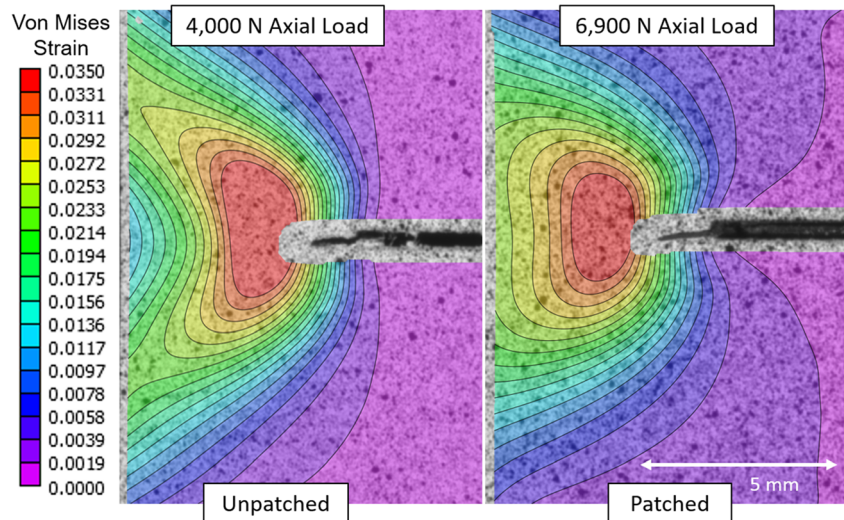
beaker and the nickel anode with a current density between 0.5 and 1.5 Amps/in^2 for 2 min. Then the sample surface was rinsed with distilled water and alcohol, then dried. Microscope images with 20× magnification with known length scale were used to study the grain structure. Grain size estimation was performed using two methods. First, the planimetric procedure with non-standard magnification is a direct calculation of the grains per square area outlined in ASTM E112 [37]. The second method approximated grains as ellipses with the major and minor axis points manually selected and measured for randomly selected grains measured from two imaged regions of the sample.

The planimetric method resulted in an ASTM grain size number of approximately 11.5 (Table 4 in Ref [37]), meaning 39.8 grains per μm^2 and an average grain diameter of 6.3 μm. The planimetric method does not convey the variability in grain structure or the difficulty measuring a 3-dimensional grain from a 2-dimensional plane. From the simplified method

of directly measured grain size the average major diameter was 10.8 ± 4.5 μm with the maximum and minimum measurements being 18.1 and 5.4 μm, respectively.

Aluminum Properties

Tensile mechanical properties of the 5052-H32 aluminum used to manufacture the small-scale CCT specimens were measured with ASTM E466 [38] sheet type dog-bone specimens following ASTM E8 [39] guidelines. Uni axial tensile stress-strain response is shown in Fig. 8 with the corresponding linear elastic modulus, Poisson's ratio, 0.2% offset yield stress (σ_{ys}), and Ramberg-Osgood elastic-plastic constants found to be consistent with existing data [28, 40]. Ramberg-Osgood parameters were fit to the data using a non linear least squares solver. Aluminum tensile properties were averaged for four specimens with resulting modulus of 70.9 ± 0.9 GPa, 0.2% offset yield strength of 116 ± 2 MPa, 0.2% offset yield strain of

Fig. 7 Longitudinal surface grain structure of 5052-H32 at 20× in gamma filtered polarized light showing grain structure size and variability in the specimen orientation
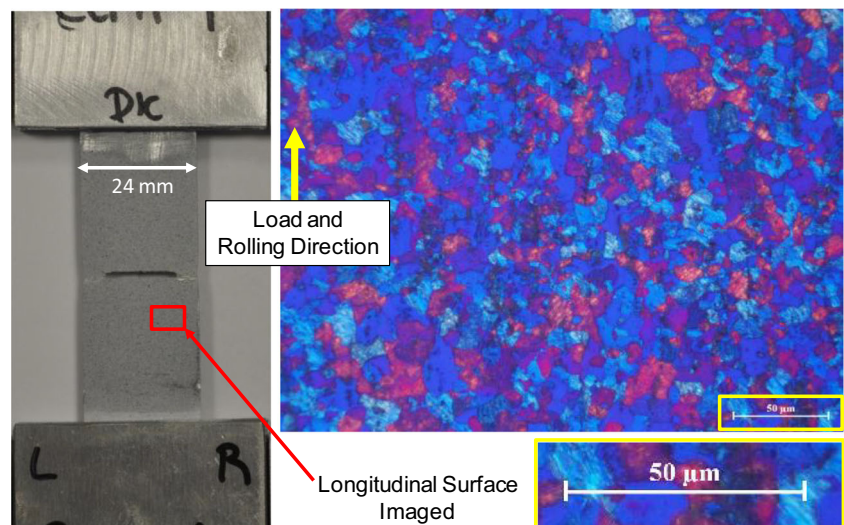
Fig. 8 Tensile test data and Ramberg-Osgood behavior approximation for aluminum 5052-H32 2.29 mm plate with axial surface strains at yield and prior to failure
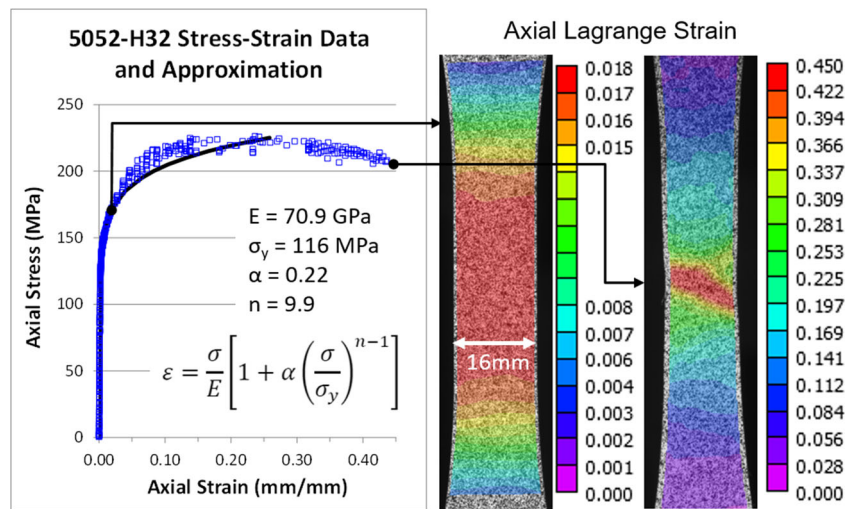
0.001800 mm/mm, and Ramberg-Osgood parameters α and n of 0.22 ± 0.06 and 9.9 ± 0.9, respectively. For comparison, the modulus of the patch is 22.2 GPa, one third the aluminum [31].

Fracture data for the 5052-H32 aluminum alloy was not readily available in literature for the plate thickness used for the small-scale CCT specimens. An initial survey of available aluminum data shows a wide range of critical stress intensity values, from 20 to 60 MPa√m, with values of 5083-H321 and 5456-H116 between 21.5 and 28.9 MPa√m.

Crack Tip Plastic Zone Estimate

Irwin's approach can be used to estimate the plastic zone radius ahead of the crack tip [17]. Assuming plane stress conditions the point at which elastic material yields is when the normal stress is equal to the yield stress from the uni-axial tension test. Under plane stress conditions this yields a second order estimate of the plastic zone diameter, r_p, in equation (3) which is derived by performing a force balance near the crack tip that includes elastic and plastic stresses. The plane stress Irwin plastic zone correction is one half of r_p and the estimated plane strain plastic zone correction is smaller by a factor of 3.

$$r_p = \frac{1}{\pi}\left(\frac{K_I}{\sigma_{ys}}\right)^2 \qquad (3)$$

The above equation provides a 1-D estimate of the plastic zone size in the plane of the crack. For isotropic materials the plastic zone shape can be estimated relative to the crack tip by setting the von Mises equivalent stress equal to the uni-axial tensile yield stress. The equivalent stress is a function of the principal stresses, which for Mode-I loading can be approximated with singular stress fields based on the stress intensity. Setting the equivalent stress equal to the yield stress results in an expression for

the plastic zone as a function of the angle from the crack plane. For plane stress the cylindrical coordinates of the plastic zone boundary at a prescribed level of mode-I stress intensity, K_I, are related using equation (4) and under plane strain conditions are related using equation (5).

$$r(\theta) = \frac{1}{4\pi}\left(\frac{K_I}{\sigma_{ys}}\right)^2\left[1 + \cos\theta + \frac{3}{2}\sin^2\theta\right] \qquad (4)$$

$$r(\theta) = \frac{1}{4\pi}\left(\frac{K_I}{\sigma_{ys}}\right)^2\left[(1-2\nu)^2(1 + \cos\theta) + \frac{3}{2}\sin^2\theta\right] \qquad (5)$$

Initial Plastic Zone Quantification

Initial plastic zone development was compared to the LEFM plastic zone size estimate in equations (3) through (5). An effective free surface K_I value at initiation of yield must be iteratively determined for a predicted plastic zone that qualitatively matches the measured shape. The measured plastic zone shape was determined by comparing the total Lagrangian 2D von Mises strain contours to the 0.2% offset strain level from tensile material tests. DIC data from the unpatched aluminum CCT specimens is shown with the upper strain contour between 0.0018–0.0019 mm/mm in Fig. 9. The plastic zone shape appears to be dominated by plane stress behavior with the influence of edge effects. The DIC results were used to measure the radial position of the plastic zone boundary for angles of 0-, 15-, 30-, 45-, 60-, 75-, and 90-degrees. At a COD of 0.024 mm and a load of 2169 N the 0.2% yield strain was exceeded forming a complete plastic zone encompassing the crack tip, which was located using a parabolic least squares fit of the vertical displacements (V) parallel to the crack plane [20].

Fig. 9 Unpatched 0.2% offset initial LEFM yield prediction and DIC measurement showing crack tip behavior dominated by plane stress
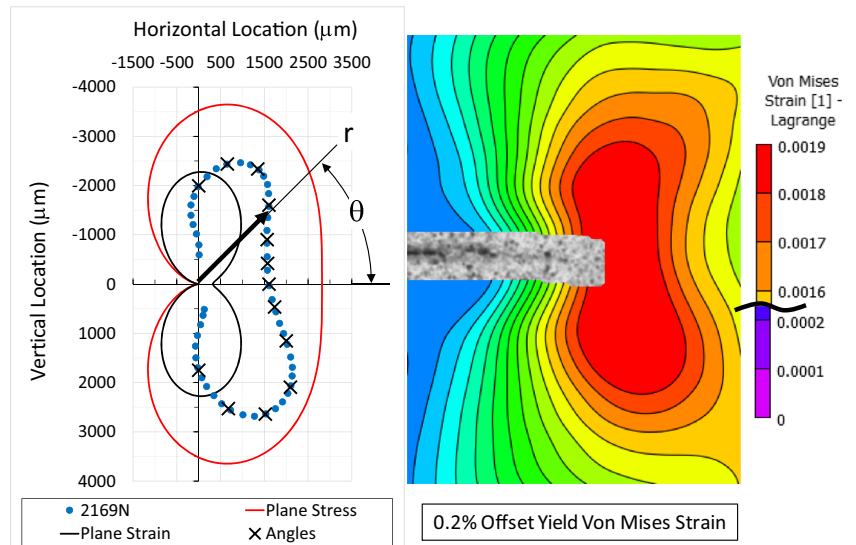

DIC data for a patched specimen is shown in Fig. 10 at a COD of 0.020 mm and a load of 2399 N. Composite patch surface reinforcement causes the qualitative strain behavior to match LEFM plane stress behavior. Though not strictly applicable due to bending caused by a one sided patch, plane stress LEFM predictions were made using equation (4). K_I was iteratively changed to qualitatively match measured DIC radial positions at both 0- and 60-degrees, the later prediction is shown in Fig. 10 (left, red line).

The region of plastic strains for both unpatched and patched plastic zones are 3 orders of magnitude larger than the measured grain size which ranged from 5.4 to 18.1 μm, supporting the assumption that the aluminum ahead of the crack tip behaves as a homogenous material during the evolution of the plastic zone.

Plastic Zone Evolution

Initial plastic zone size and shape were established using total 2D free surface von Mises strain contours and a quantitative comparison of the large strain regions as a function of COD to support the observed improvement in the patched load versus COD behavior. In the vicinity of the crack tip, the large strain area will be estimated, not directly measured, using the triangles created between the radial large strain positions as illustrated in Fig. 11. For the 0- to 90-degree quarter, the summation of all the triangles provides an area for comparison assuming the change in this area is representative of the total change in area defined by the selected large strain magnitude. The initial comparison was performed at the plastic strain limit, however as load increases the plastic strain region extends beyond the DIC area of interest (AOI), which requires measuring the radial positions at large strain

Fig. 10 Patched CCT specimen 0.2% offset initial LEFM yield prediction and DIC measurement showing patched crack tip behavior similar to plane stress
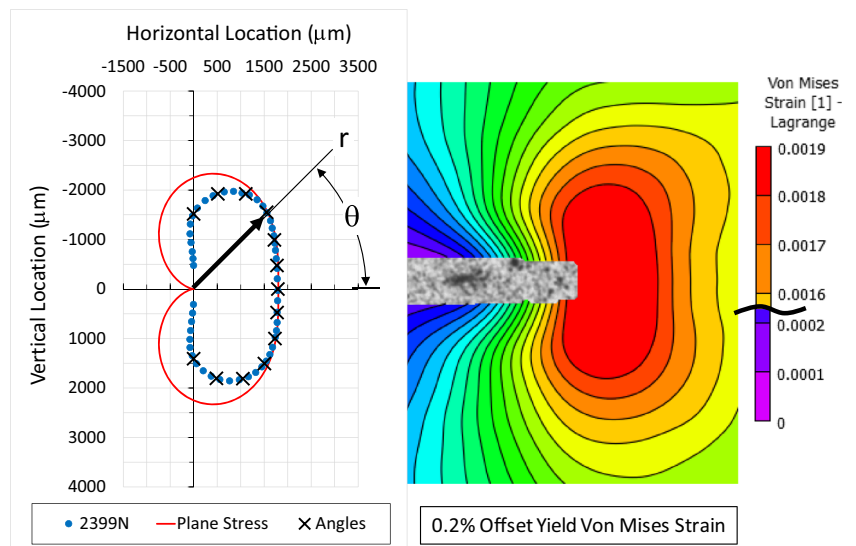
Fig. 11 Load and COD magnitudes studies (L) and the large strain region area definition (R) for unpatched to patched comparison
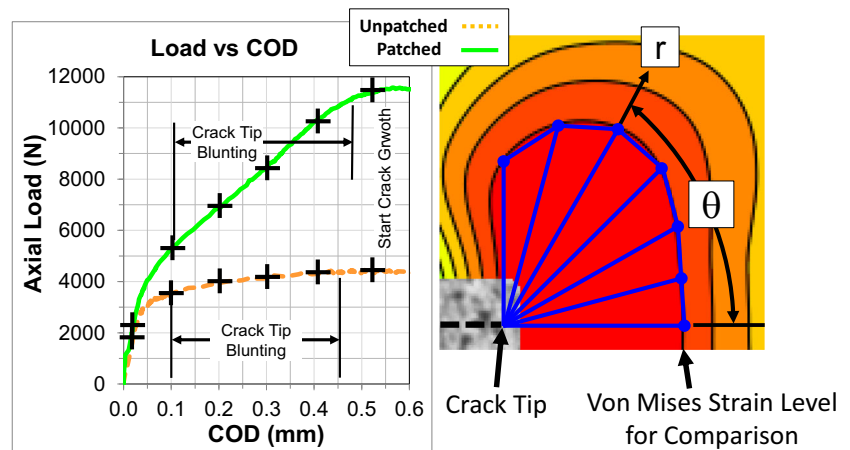
magnitudes unique to each COD. The large strain magnitudes were selected such that each radial path had a distinguishable large strain radial position. The load and COD magnitudes studied are indicated by the "+" marks on the load versus COD plot in Fig. 11 and fall within the linear elastic response range, the crack blunting stage and initiation of crack growth before the peak load is achieved.

In addition to the crack tip behavior the centerline strain near the notch is also investigated to quantify the level of load bridging for the patched specimen. Centerline von Mises strain is averaged over a 1 mm² area 4 mm above the center of the machined notch, as shown in Fig. 12, which is outside the effects of notch edge correlation and within the stress shadow associated with the load path around a notch.

In subsequent figures, the DIC AOI incorporates the entire width of the specimen with the exception of a half subset width (0.17 mm) at the left and right edges. The speckle pattern adjacent to the top and bottom of the notch had errors with a magnitude of 0.000700 mm/mm, an average bias of 0.000500 mm/mm, and a standard deviation of ±0.000200 mm/mm. Assessment of speckle pattern application was focused on the region ahead of the crack tip, where bias and error were an order of magnitude lower at 0.000050 ± 0.000015 mm/mm. Similar results were achieved for the centerline strain region with the speckle pattern achieving strain errors of 0.000080 ± 0.000030 mm/mm and 0.000045
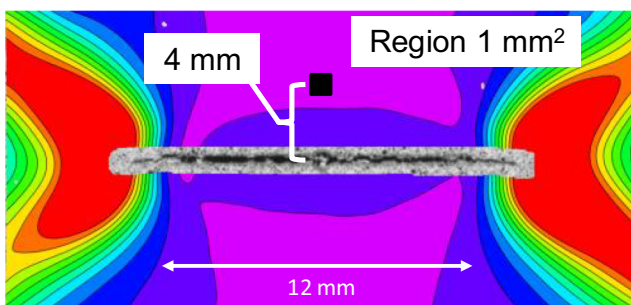
± 0.000010 mm/mm for the unpatched and patched specimens, respectively. In the following figures the strain contours shown are uniquely defined for each COD and consistent for images in that figure.

From the previous discussion the fully formed plastic zone occurs at a load of 2170 N for the unpatched and 2400 N for the patched specimen, which correspond to COD's of 0.024 mm and 0.021 mm, respectively. Studying the evolution as a function of COD demonstrates that the additional bending present in the patched specimen leads to the development of plastic strains at a COD of 0.021 mm (Left of Fig. 13), the point before plastic strains develop on the unpatched specimen surface. Increasing COD to 0.024 mm, both the unpatched and patched specimens exhibit fully developed plastic zones (Right of Fig. 13). Here the load carried by the patched specimen is 24% greater with a plastic zone area that is three times greater. During this stage of loading the specimen deflects out-of-plane as the patched centroid approaches the load line, which is assumed to be less than 0.36 mm. The plastic strain radial positions are listed and compared in Table 1. Composite patch reinforcement increases the radial position of the plastic zone boundary due to bending and surface reinforcement.

Qualitatively the composite patch reinforces the ligament ahead of the crack tip in both the axial and transverse directions, while the unpatched specimen shows the influence of edge effects in the form of a plastic zone shape that does not match theoretical plane stress predictions. From the linear elastic response limit to the initiation of crack blunting the large strain field height is constrained while the width increases due to transverse patch stiffness. Crack blunting initiates at a COD of approximately 0.11 mm for both the unpatched and patched specimens, based on observations from unprocessed static images. Comparison of the large strain region boundaries was performed at a von Mises magnitude of 0.011500 mm/mm with resulting strain fields and the measured large strain boundary radial positions shown in Fig. 14. The composite patch increased the load 52% and the area

Fig. 12 Centerline strain region definition to study the effect of load bridging for patched specimens

Fig. 13 Comparison of plastic strain at COD = 0.021 mm (L) and 0.024 mm (R). patched surface plastic strain occurs first, then the patched specimen maintains a greater area of plastic strain
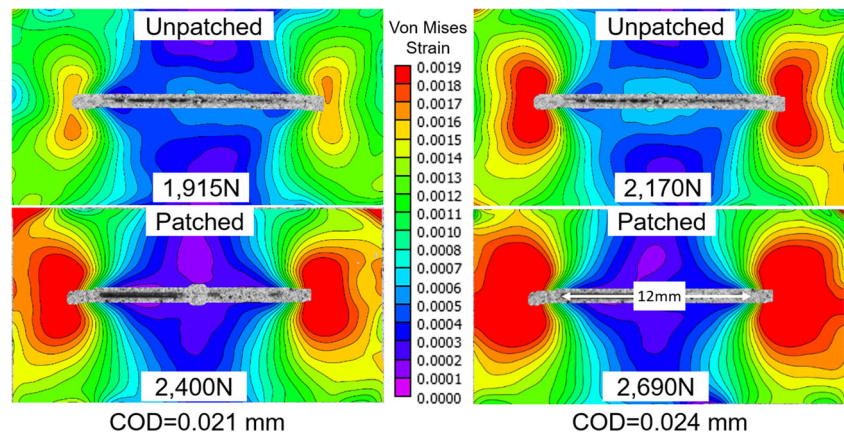
of large strain by 69%. Out-of-plane bending reached a maximum, as indicated by the stabilization of the load versus COD response slope beyond a COD of 0.11 mm. As the influence of bending decreases, the magnitude of large area change due to the patch also decreases. Locally, the axial and transverse patch reinforcement increases the large strain area width 75% and the overall height 5–10%.

As COD increases beyond 0.11 mm the influence the patch has on the free surface crack tip behavior decreases. The 2D von Mises large strain magnitudes used to establish the large strain area for CODs of 0.31, 0.41, and 0.55 mm were 0.034, 0.044, and 0.065 mm/mm, respectively. The large strain area ahead of the unpatched crack tip exceeds that of the patched specimen for CODs greater than 0.41 mm where crack blunting transitions to the initiation of crack growth prior to achieving peak loads with strain field comparison shown in Fig. 15 at a COD of 0.55 mm. Here the load is 160% greater and the patched large strain area is now 25% smaller. Beyond a COD of 0.31 mm the large strain areas for unpatched and patched specimens show qualitatively similar shape and quantitatively similar size. Local crack tip strain contours from a COD of 0.21 mm to those shown for a COD of 0.55 mm are similar, with the specimen edge effects becoming evident in the patched strain contours. This indicates dominance of tensile behavior ahead of the crack tip compared to bending and a reduced influence of the patch on the free surface.

Centerline 2D von Mises strains show additional effects of the patch. Qualitatively the width of the centerline strain shadow due to the load passing ahead of the crack tip has decreased and reduced strain gradient magnitudes at the edge of the large strain areas. Quantitatively the load bridging due to the patch increases the average centerline von Mises strain. From the linear elastic response limit the average centerline strain for the patched specimen increases from approximately 0.000250 mm/mm to a local maximum of 0.002700 mm/mm beyond a COD of 0.41 mm, while the unpatched specimen strain magnitude remains constant at a nominal level of 0.000250 ± 0.000050 mm/mm for CODs from 0.024 to 0.55 mm. Composite patch reinforcement transfers enough load across the notch for the centerline aluminum to achieve plastic von Mises strain on the surface. Note here that the von Mises strains are not zero along the centerline of the unpatched specimen because of transverse strain contributions. Axial strain (ε_{yy}) magnitudes, however, are nominally zero within the static image bias and error for the range of CODs studied and the patched specimen axial strains are 35–50% smaller than the 2D von Mises strains above a COD of 0.20 mm due to transverse strain contributions.

Summary of Unpatched Versus Patched Free Surface Response

In summary, two primary factors contribute to the improved load response and the similarity in the failure response as a function of COD. First, load sharing of the patch reinforcement, shown by the increase in centerline strain, contributes to the additional load capacity. Second, the increase in large strain area measured above the plastic strain limit is due to the patch reinforcement distributing strain ahead of and in the wake of the crack tip contributing to both the additional load and COD capacity. Global load response and strain fields on the aluminum

Table 1 Radial positions comparison for yield boundary of fully developed plastic zone (COD = 0.024 mm)

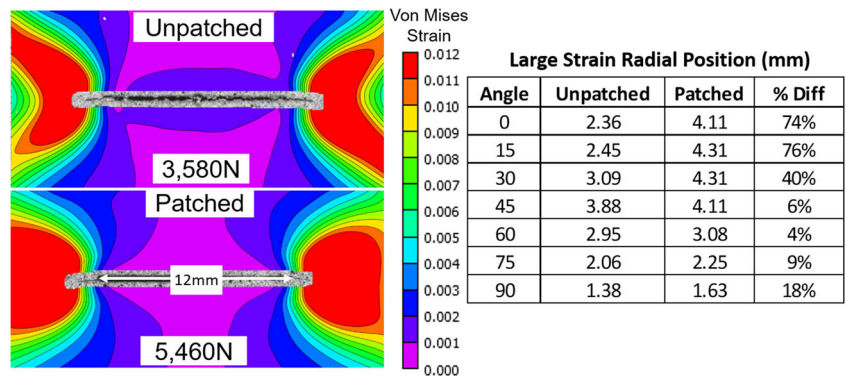| Angle	Unpatched	Patched	%Diff
0	1.58	4.20	166%
15	1.62	3.70	128%
30	1.78	3.87	118%
45	2.24	4.03	80%
60	2.65	3.59	36%
75	2.48	3.16	28%
90	1.93	2.59	34%

Fig. 14 Comparison of large strain fields at COD = 0.11 mm (L) and the large strain boundary radial positions at 0.011500 mm/mm (R) showing increased large strain area on the free surface with a bonded patch

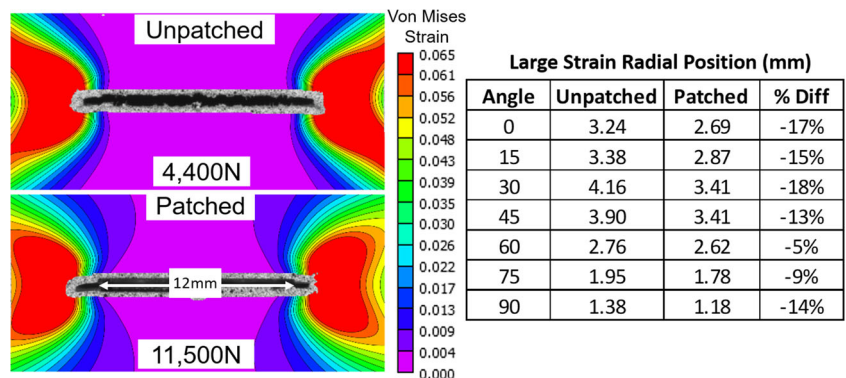| Large Strain Radial Position (mm)			
Angle	Unpatched	Patched	% Diff
0	2.36	4.11	74%
15	2.45	4.31	76%
30	3.09	4.31	40%
45	3.88	4.11	6%
60	2.95	3.08	4%
75	2.06	2.25	9%
90	1.38	1.63	18%

free surface show the effects of the one-sided patch reinforcement. Initially, the patched specimen developed plastic strains prior to the unpatched specimen primarily due to out-of-plane bending. As load and COD increase three trends due to the patch reinforcement emerged: load capacity increase is proportional to COD, local crack tip large von Mises strain area on the free surface is inversely proportional to COD, and average centerline von Mises strain increases proportionally with COD as shown in Fig. 16. For CODs of 0.4 mm and smaller the patch reinforcement increases the region of large strain with patch reinforcement influencing the free surface response. As COD increases beyond 0.4 mm large strain area of the unpatched specimen is greater than that of the patched specimen. Average centerline strain increases because of the load carrying ability of the patch reinforcement, however as the COD increases beyond 0.4 mm the influence of the patch on free surface centerline strains reaches a plateau at a 2D von Mises strain magnitude of 0.0027 mm/mm, which exceeds the plastic strain level.

The unpatched specimen strain field at the crack tip is influenced by both the crack tip singularity and tensile ligament behavior and has an assumed symmetric through thickness response. Addition of the patch reinforces the transverse response of the aluminum ligament and offsets the neutral axis of the specimen introducing out-of-plane bending and an asymmetric response with through thickness behavior gradient at the crack tip where free surface stress intensity can nominally be 4× that of the patched surface, as shown by Wang and Rose [9]. With theoretical through thickness behavior and the global load and free surface strain responses as a function of COD one can infer details about the specimen response. The COD at which the load goes through the patched specimen centroid is where the load as a function of COD slope is constant beyond the non linear region, which matches assumptions made by Baker to develop simplified equations to represent geometrically non linear response [8]. From this point, the bending contribution remains constant and the tensile behavior of the section advances with the free surface seeing more load than the patched surface and therefor governing the failure response. Further investigation of the through thickness behavior is beyond the scope of this paper and requires detailed 3D finite element analysis (FEA) techniques.

Fig. 15 Comparison of large strain fields at COD = 0.55 mm (L) and large strain boundary radial positions at 65,000 με (R) showing large strain areas indicating decreased influence of the patch on the free surface with edge effects and qualitatively similar shapes

Large Strain Radial Position (mm)			
Angle	Unpatched	Patched	% Diff
0	3.24	2.69	-17%
15	3.38	2.87	-15%
30	4.16	3.41	-18%
45	3.90	3.41	-13%
60	2.76	2.62	-5%
75	1.95	1.78	-9%
90	1.38	1.18	-14%

Fig. 16 Increase in load, large strain area, and patched centerline free surface strain as a function of COD showing load capacity and centerline strain proportional to COD and large strain area inversely proportional to load
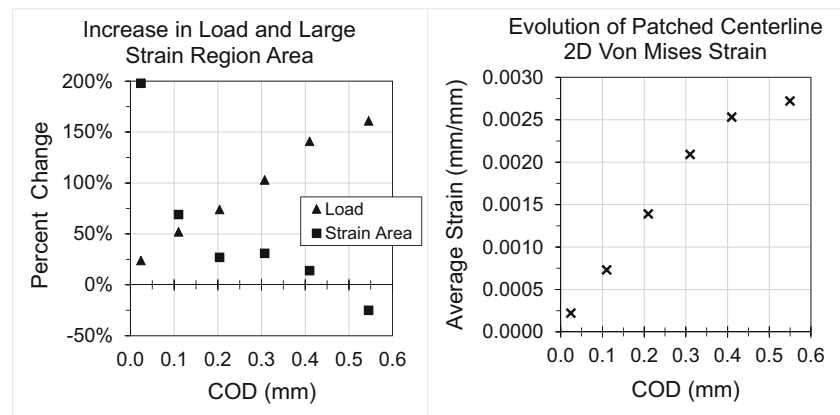
Conclusions

The primary focus of this paper was to document the measurable effect that one-sided adhesively bonded low modulus E-Glass/Epoxy composite patch has on development of the crack tip plastic zone for small-scale aluminum CCT specimens loaded monotonically in tension until failure. Full-field free surface displacements and total von Mises strains measured during loading for both unpatched and patched specimens allowed qualitative and quantitative comparison of responses. Uncertainty exists for the small data set, however behavior correlated for like specimens and variability of a larger data set is assumed to not significantly affect relative comparisons. Load response and the fracture progression until peak load of both the unpatched and patched specimens were a function of the COD independent of the patch reinforcement. For both specimen types, the crack blunting stage initiated at a COD of 0.11 mm and concluded at a COD of 0.41 mm. Crack blunting transitions to the initiation of crack growth prior to developing peak load for both specimen types, which occurred at a COD of 0.57 mm with the patched load being 160% greater. Crack growth and gradual load drop then specimen failure followed peak load. Based on static images, the patch disbonded at a COD of 1.0 mm resulting in a sudden load drop. Specimen failure continued with aluminum fracture, however, the COD magnitude was 20% greater for the same aluminum specimen response load. Direct correlation of fracture behavior prior to the peak load indicates patched specimen failure can be predicted using unpatched specimen failure COD. Increased load capacity and centerline strain of the patched specimen is proportional to COD while the increase in free surface large strain area is inversely proportional to COD. Additional patched load and displacement capacity correlates with load carried by the patch and the accumulation of increased large strain area and plastic deformation on the free surface of the aluminum. True through thickness adhesive behavior is outside the scope of this paper, however free surface centerline strains indicate an effective transfer of load between the aluminum and the patch until patch disbond.

The grain structure of 5052-H32 was characterized using a LOM with gamma filtered polarized light. Grains of this alloy have an approximate 2D surface major diameter of 10.8 ± 4.5 μm with the maximum and minimum measurements being 18.1 and 5.4 μm, respectively. Alloy grain structure was compared to the measured plastic zone size and shape. The unpatched plastic zone shape indicates edge effects and did not perfectly match plane stress conditions with radial positions between 1500 and 2800 μm. Patch reinforcement reduces edge effects and the plastic zone shape correlated well with plane stress behavior with radial positions between 1700 and 2100 μm. The difference between the region of interest and the grain size is greater than two orders of magnitude, therefore the material responds as a homogenous material during evolution of the plastic zone. Future research will focus on investigating the through thickness behavior of the patched specimen utilizing 3D FEA, correlating measured surface behavior with inelastic strain energy release rate and predicting ultimate specimen failure.

References

1. Volkerson O (1938) Die Niektraft in Zugbeanspruchten mit Kontanten Laschenquerschritten. Luftfahrtforsch. 5:41–47
2. Goland M, Reissner E (1944) The stress in cemented joints. J Appl Mech 11(1):A17–A27
3. Hart-Smith LJ (1973) Adhesive-bonded double-lap joints. NASA CR-112235
4. Hart-Smith LJ (1973) Adhesive-bonded single-lap joints. NASA CR-112236

5. Tsai GC, Shen SB (2004) Fatigue analysis of cracked thick aluminum plate bonded with composite patches. Compos Struct 64:79–90. https://doi.org/10.1016/S0263-8223(03)00216-2

6. Jones R, Chiu WK (1999) Composite repairs to cracks in thick metallic components. Compos Struct 44:17–29. https://doi.org/10.1016/S0263-8223(98)00108-1

7. Duong CN (2009) Design and validation of composite patch repairs to cracked metallic structures. Comp Part A 40:1320–1330

8. Baker AA, Rose LR, Jones R (2002) Advances in the bonded composite repair of metallic aircraft structures, vol 1. Elsevier, New York

9. Wang CH, Rose LRF (1999) A crack bridging model for bonded plates subjected to tension and bending. Int J Solids Struct 36:1985–2014. https://doi.org/10.1016/S0020-7683(98)00070-5

10. Noland JM, Hart DC, Udinski EP, Sielski RA (2013) Initiatives in bonded ship structural repairs. ASNE Fleet maintenance and modernization symposium, San Diego, CA. https://doi.org/10.1097/PRS.0b013e3182a8066b

11. Baker AA, Rose LR, Walker KE, Wilson ES (1999) Repair substantiation for a bonded composite repair to F111 lower wing skin. Appl Compos Mater 6:251–267. https://doi.org/10.1023/A:1008805813470

12. Muller R, Fredell R (1999) Analysis of multiple bonded patch interaction simple design guidelines for multiple bonded repairs in close proximity. Appl Compos Mater 6:217–237. https://doi.org/10.1023/A:1008869910744

13. Hart DC (2016) Aluminum sensitization and application of laminated composite patch repairs. In: Proc. Society for Experimental Mechanics XIII international congress and exposition on experimental applied mechanics, experimental dynamic behavior: integrating experimental mechanics, Orlando, FL, 2016

14. Nahshon K, Hoffman WA, Ullagaddi CB (2014) Characterization of structural scale ductile fracture of aluminum panels using digital image correlation. In: Proc. 214th Annu Conf On Exp Appl Mech

15. Hart DC, Udinski EP, Hayden MJ, Liu X (2014) Fatigue performance and analysis of composite patch repaired cracked aluminum plates. In: Sh. Struct. Comm., Sustainability and Stewardship, Vessel Safety and Longevity Through Research, Linthicum Heights, MD

16. Hutchinson JW (1968) Singular behaviour at the end of a tensile crack in a hardening material. J Mech Phys Solids 16:13–31

17. Anderson TL (1995) Fracture mechanics fundamentals and applications, Second ed., CRC Press LLC. https://doi.org/10.1002/jhrm.5600150304

18. Rice JR, Rosengren GF (1968) Plane strain deformation near a crack tip in a power-law hardening material. J Mech Phys Solids 16:1–12

19. Sutton MA, Orteu JJ, Schreier HW (2009) Image correlation for shape, motion, and deformation measurements. Springer LLC

20. Bruck HA (1989) Analysis of 3-D effects near the crack tip on Rice's 2-D J-integral using digital image correlation and smoothing techniques. Thesis, University of South Carolina

21. Sutton MA, Turner JL, Chao YJ, Bruck HA, Chae TL (1992) Experimental investigations of three dimensional effects near a crack tip using computer vision. Int J Fract 53:201–228

22. Yoneyama S, Arikawa S, Kusayanagi S, Hazumi K (2014) Evaluating J-integral from displacement fields measured by digital image correlation. Strain 50:147–160. https://doi.org/10.1111/str.12074

23. Hickey WF (2011) An investigation into the failure of aluminum alloys. Thesis, University of Texas at Austin. https://doi.org/10.1055/s-0031-1280671

24. Becker TH, Mostafavi M, Tait RB, Marrow TJ (2012) An approach to calculate the J-integral by digital image correlation displacement field measurement. Fatigue Fract Eng Mater Struct 35:971–984. https://doi.org/10.1111/j.1460-2695.2012.01685.x

25. Fernandez-Zuniga D, Kalthoff JF, Fernandez-Canteli A, Grasa J, Doblare M (2004) Three dimensional finite element calculations of crack tip plastic zones and KIC specimen size requirements. In: European Conference on Fracture, Stockholm, Sweden

26. Hamam R, Hild F, Roux S (2007) Stress intensity factor gauging by digital image correlation: application in cyclic fatigue. Strain 43:181–192. https://doi.org/10.1111/j.1475-1305.2007.00345.x

27. Dadkhah MS, Kobayashi AS, Morris WL (1992) Crack-tip displacement fields and JR-curves of four aluminum alloys. In: fracture mechanics: twenty-second symposium (volume 11), ASTM STP 1131, Philadelphia

28. Dadkaha MS, Kobayashi AS (1990) Further studies on the HRR field of a moving crack, an experimental analysis. Int J Plast 6:635–650. https://doi.org/10.1016/0749-6419(90)90036-E

29. May GB, Wang FX, Kobayashi AS (1993) Two-parameter crack tip field associated with stable crack growth in a thin plate - a hybrid analysis. Mechanical engineering College of Engineering University of Washington, technical report for Office of Naval Research UWA/DSE/TR-93/71. https://doi.org/10.1016/0378-1119(93)90107-e

30. Dadkhah MS, Kobayashi AS (1998) HRR field of a moving crack, an experimental analysis. Eng Fract Mech 34:253–262

31. Hart DC, Bruck HA (2018) Low Modulus composite patched aluminum center crack tension specimen DIC surface displacements compared with predictions. In: Society for Experimental Mecahnics Annual Conference and Exposition on Experimental Applied Mechanics, Greenville, SC

32. Correlated Solutions Inc. (2018) Vic-2D v6 Reference Manual. Correlated Solutions Inc., Irmo, SC 29063 https://www.correlatedsolutions.com. https://doi.org/10.1016/S0140-6736(18)33054-X

33. O'Shaughnessy TG (1985) ALCOA 5000-series alloys suitable for welded structural applications. Aluminum company of America applications engineering division, green letter no. 143 second revision, Pennsylvania. https://doi.org/10.1103/physreva.32.3073

34. Hatch JE (ed) aluminum properties and physical metallurgy. ASM International

35. ASTM E399–08 (2008) Standard test method for linear-elastic plane-strain fracture toughness KIC of metallic materials. American Society for Testing and Materials International, Conshohoken

36. ASTM E407–07 (2007) Standard practice for microetching metals and alloys. American Society for Testing and Materials International, Conshohoken

37. ASTM E112–13 (2013) Standard test methods for determining average grain size. American Society for Testing and Materials International, Conshohoken

38. ASTM E466–07 (2007) Standard practice for conducting force controlled constant amplitude axial fatigue tests of metallic materials. American Society for Testing and Materials International, Conshohocken

39. ASTM E8M-08 (2008) Standard test methods for tension testing of metallic materials. American Society for Testing and Materials International, Conshohocken

40. Ozturk F, Totos S, Kilic S (2008) Evaluation of tensile properties of 5052 type aluminum-magnesium alloy at warm temperatures. Arch Mater Sci Eng 34:95–98